Research Article | Open Access

Soft Science

Jin *et al. Soft Sci.* **2026**, *6*, 60 **DOI:**10.20517/ss.2026.60

Privacy-preserving gait biometrics via synchronous mechanical and bioelectrical co-sensing and ciphertext-domain inference

Yexi Jin[1], Ruolin Wang[2], Jianyu Lin[1], Yu Lu[1], Jing Zhang[1], Xingwen Zhou[1], Baijie Cheng[2,*], Liguo Chen[1,*]

Keywords:
Low hysteresis, gait recognition, multimodal sensors, flexible wearable electronics, machine learning

Citation: Jin, Y.; Wang, R.; Lin, J.; Lu, Y.; Zhang, J.; Zhou, X.; Cheng, B.; Chen, L. Privacy-preserving gait biometrics via synchronous mechanical and bioelectrical co-sensing and ciphertext-domain inference. *Soft Sci.* **2026**, *6*, 60. https://dx.doi.org/10.20517/ss.2026.60

Received: 27 Mar 2026
First Decision: 20 Apr 2026
Revised: 2 May 2026
Accepted: 22 May 2026
Published: 6 Jul 2026

Academic Editors:
Yu Song, Kuniharu Takei
Copy Editor:
Xing-Yue Zhang
Production Editor:
Xing-Yue Zhang

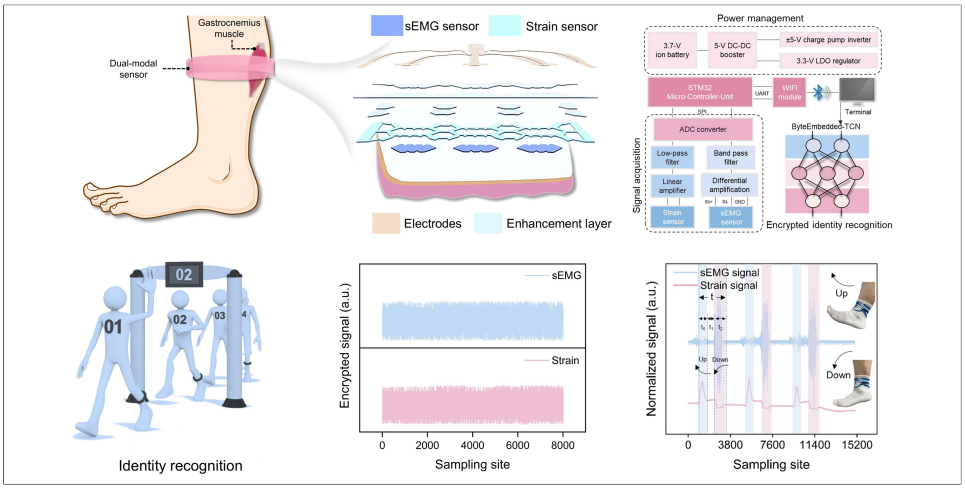

Abstract

Gait information is rooted in muscle contraction dynamics and neuromuscular regulation, and represents a reliable biometric. However, mechanical and bioelectrical signals acquired using conventional wearables are prone to replication and forgery during storage and transmission. Moreover, the degradation of recognition performance under standard encryption can occur due to limited feature dimensionality and fidelity. In this study, we present a spatiotemporally synchronous strain-surface electromyography (sEMG) co-sensing system (S-SESS), which co-locates and phase-aligns kinematic and neuromuscular signals from the gastrocnemius to deliver secure gait recognition. The strain sensing unit achieves a low hysteresis (1.6% at 100% strain) and high cyclic fidelity (> 10,000 cycles) using hierarchical supramolecular aggregates with multiple hydrogen bonds and dynamic π-π stacking that ensure precise phase tracking. The adaptive sEMG unit exhibits high interfacial conformity, suppresses motion artifacts, and achieves a signal-to-noise ratio (SNR) greater than 40 dB. The bimodal features are locally encrypted using the Advanced Encryption Standard-128 (AES-128) algorithm and processed directly in the ciphertext domain via a dedicated ByteEmbedded Temporal Convolutional Network

[1]School of Mechanical and Electrical Engineering, Soochow University, Suzhou 215000, Jiangsu, China.
[2]College of Chemistry and Chemical Engineering, Donghua University, Shanghai 201620, China.

[*]**Correspondence to:** Dr. Baijie Cheng, College of Chemistry and Chemical Engineering, Donghua University, Shanghai 201620, China. E-mail: 1222004@mail.dhu.edu.cn; Prof. Liguo Chen, School of Mechanical and Electrical Engineering, Soochow University, Suzhou 215000, Jiangsu, China. E-mail: chenliguo@suda.edu.cn

(ByteEmbedded-TCN). This directly maps ciphertext streams into byte-embedded sequences and leverages causal and dilated convolutions to construct multi-scale receptive fields for temporal alignment and classification. The end-to-end framework achieves 89.7% ± 1.2% gait identification accuracy under encryption. The findings of this study provide a privacy-preserving wearable paradigm for trustworthy identity authentication.

INTRODUCTION

Biometric methods, including fingerprints, irises, facial features, and DNA, are highly distinctive but also sensitive and irrevocable with consequent risks of data leakage and misuse when collected and shared at scale[1,2]. In contrast, gait recognition as a behavioral biometric, is non-invasive, requires no active cooperation, and enjoys high user acceptance, representing a suitable solution for health monitoring, security, and immersive interaction[3]. Flexible wearables located on the sole, ankle, or calf can capture external kinematics and muscle bioelectrical activity, enabling continuous, individualized recognition in complex environments[4-6]. Machine learning methods have achieved high accuracy in gait recognition, but the majority of systems rely on transmitting plaintext trajectories or waveforms between edge and cloud, which are vulnerable to forgery and replay attacks due to their simplicity and ease of replication[7]. Consequently, there is a pressing need for recognition systems that preserve accuracy while ensuring data privacy.

Current gait recognition methods typically depend on individual biological signals, such as pressure, strain, surface electromyography (sEMG), accelerometer data, gyroscope readings, or force sensors[8,9]. These signals offer different insights regarding gait: pressure and strain capture mechanical forces and deformations, EMG reflects muscle activation patterns, and accelerometer and gyroscope data measure movement dynamics and postural changes[10]. However, gait is inherently a multi-dimensional process involving mechanical and bioelectrical signals, where an integrated approach is essential to gain a full understanding of gait dynamics[11]. Published studies have focused on the use of one type of signal, often neglecting the interaction between mechanical and bioelectrical signals.

Multimodal fusion is a promising approach to improve the accuracy and robustness of gait recognition, but its effectiveness is highly dependent on the fidelity of each signal modality. Significant efforts have been directed at engineering the electrode-skin interface by applying novel materials and optimized geometries[12-14]. Nevertheless, mechanical sensors exhibit hysteresis, energy loss, and reduced sensitivity during cyclic deformation, which can lead to signal distortion or drift, ultimately compromising gait recognition precision[15-17]. In the case of bioelectrical signals, the primary challenges include electrode signal-to-noise ratio, interfacial impedance, and insufficient dynamic compliance[18]. These issues are more pronounced under repeated deformation or high load, resulting in signal distortion and unstable acquisition[19]. The fidelity issues associated with the mechanical and bioelectrical signals must be addressed to ensure the requisite data quality for effective multimodal fusion.

This work presents a spatiotemporally synchronized strain-surface electromyographic sensing system (S-SESS) that is designed to enable high-precision gait recognition in encrypted environments. The strain channel utilizes supramolecular aggregates formed by the dimerization and π-π stacking of 2-ureido-4[1H]-pyrimidinone (UPy) moieties as cross-linkers. The deep eutectic solvent (DES) flexible polymer is reinforced by strong hydrogen bonding and rapid π-π stacking dissociation/reassembly to achieve the necessary toughness (5.61 $MJ \cdot m^{-3}$) and low hysteresis (1.6% at 100% strain), maintaining stable electrical signals over 10,000 cycles. The bioelectrical channel features a dynamically adaptive conductive network with a high interfacial compliance, effectively reducing impedance and transmission loss, and achieving high-fidelity surface electromyographic recording with a signal-to-noise ratio (SNR) > 40 dB. Applying kirigami

structuring to the strain unit, and embedding sEMG gels in the pores, the device achieves a coplanar bimodal configuration. Stress concentration, driven by modulus mismatch, amplifies the strain fields, enhancing sensitivity under an identical load. Bimodal data are encrypted locally using the Advanced Encryption Standard-128 (AES-128) algorithm. Classification without decryption is enabled by a ByteEmbedded Temporal Convolutional Network (ByteEmbedded-TCN) that embeds ciphertext streams and generates multi-scale receptive fields via causal dilated convolutions. A shared embedding with coupling constraints serve to enhance cross-modal discriminability. Applying this pipeline, we have achieved 89.7% ± 1.2% identity recognition accuracy in the ciphertext domain. The proposed framework demonstrates ciphertext-domain deep learning that can enhance privacy and robustness, providing a secure paradigm for "real-world" wearable biometrics.

EXPERIMENTAL

Materials

N-(3-sulfopropyl)-*N*-(methacryloxyethyl)-*N*,*N*-dimethylammonium betaine (DMAPS, > 99%), zirconium oxychioride ($ZrOCl_2$, 98%), ethylene glycol (EG, > 99%), choline chloride (ChCl, > 99%), and 2-hydroxy-4-(2-hydroxyethoxy)-2-methylpro-piophenone (photo-initiator 2959, 98%) were purchased from Macklin Biochemical Co., Ltd. Methacrylic acid (MAA, > 99%), acrylic acid (AA, > 99%), 4-hydroxybutyl acrylate (4HBA, ≥ 99%), 1,6-diisocyanatohexane (HDI, ≥ 98%), *N*-*N*'-methylene diacrylamide (MBAA, 99%), 2-amino-4-hydroxy-6-methylpyrimidine (> 98%), and dibutyltin dilaurate (DBTDL, ≥ 95%) were purchased from Aladdin Biochemical Technology Co., Ltd. Hexane (≥ 97%), trichloromethane (≥ 99%) and dichloromethane (≥ 99.5%) were purchased from Shanghai Youshi Chemical Co., Ltd. The commercial Ag/AgCl gel electrode was obtained from 3 M Company. Ecoflex 00-30 silicone rubber was purchased from Smooth-On company (USA). The polydimethylsiloxane (PDMS) base and curing agent were purchased from Dow Corning Co., Ltd.. The 4-{6-[3-(6-methyl-4-oxo-1,4-dihydropyrimidin-2yl)ureido]hexyl carbamoyloxy}butyl acrylate (UPy-HBA) was prepared in accordance with previously reported procedures[20,21]. All the chemicals were used without further processing.

Synthesis of compound 1 (UPy-NCO)

As shown in Supplementary Figure 1A, UPy-NCO was synthesized following a procedure reported in the literature[20]. The 2-amino-4-hydroxy-6-methylpyrimidine (10 mmol, 1.25 g) was mixed with 6 equiv. HDI (60 mmol, 10.11 g). The mixture was stirred in a nitrogen atmosphere at 90 °C for 24 h. Following rection, the mixture was washed with sufficient hexane to remove unreacted HDI. The product was dried at 50 °C under vacuum overnight to obtain a white powder (2.82 g, yield, 96%). The ^{1}H nuclear magnetic resonance (NMR) spectrum ($CDCl_3$, room temperature, 600 MHz, δ (ppm)) of UPy-NCO is presented in Supplementary Figure 1B: 13.11 (s, 1H), 11.86 (s, 1H), 10.16 (d, J = 4.7 Hz, 1H), 5.82 (s, 1H), 3.31-3.25 (m, 4H), 2.23 (s, 3H), 1.67-1.56 (m, 4H), 1.42-1.38 (m, 4H).

Synthesis of compound 2 (UPy-HBA)

The synthesis of UPy-HBA employed a modified procedure outlined in the literature[21]. The UPy-NCO (5 mmol, 1.46 g) and 4-hydroxybutyl acrylate (5.5 mmol, 0.79 g) were added to dried CH_3Cl (50 mL). Then, 0.04 mL of catalyst (DBTDL) was added, and the solution stirred at room temperature for 24 h under a nitrogen atmosphere. The solvent was removed under reduced pressure, and the residue was washed with excess acetone and dried in vacuum, generating 2.02 g of a white solid (yield 89%). The ^{1}H NMR spectrum [CDCl3, room temperature, 600 MHz, δ (ppm)] of UPy-HBA is shown in Supplementary Figure 1C: 13.10 (s, 1H), 11.83 (s, 1H), 10.16 (t, J = 5.1 Hz, 1H), 6.39-6.34 (m, 1H), 6.14-6.07 (m, 1H), 5.82-5.78 (m, 2H), 4.92 (s, 1H), 4.14-4.06 (m, 4H), 3.30-3.08 (m, 4H), 2.15 (s, 3H), 1.72-1.34 (m, 12H).

Preparation of the DES

Choline chloride (ChCl) and ethylene glycol (EG) were dried in a vacuum oven at 60 °C for 48 h. The ChCl and EG were then mixed at a molar ratio of 1:2, and the mixture was transferred to a flask and stirred at 90 °C for 2 h until a homogeneous colorless liquid formed. The liquid was removed in a vacuum oven at 80 °C for 24 h; the resulting DES is denoted as ChCl/EG. The water content (0.16 wt.%) of the DES was determined by Karl Fischer titration.

Preparation of PMDU eutectogels

The PMDU eutectogels for use in strain sensing were fabricated using DES as the solvent, MAA and DMAPS as comonomers, and UPy-HBA as the cross-linker. The procedure for preparing the $PMDU_3$ eutectogel is as follows: 0.143 g (0.3 mmol) UPy-HBA was added to 5.26 g (0.02 mol) DES and stirred at 90 °C until clear and transparent. Then, 2.58 g (0.03 mol) MAA, 2.79 g (0.01 mol) DMAPS, and 0.009 g (0.04 mmol) I2959 were added to the solution and mixed thoroughly. The mixture was injected into a glass mold coated with a release film. Photopolymerization was conducted under UV irradiation (365 nm, 30 W) for 10 min in a nitrogen atmosphere. The resulting transparent eutectogel is denoted as $PMDU_3$. By adjusting the molar content of UPy-HBA, a series of $PMDU_x$ eutectogels (x = 0, 1, 2, 3, 4) was obtained.

Preparation of sEMG gel

Based on previous research, an adaptive eutectogel with a high interfacial compliance was prepared. A combination of 0.4 mol AA, 0.1 mol DMAPS, 0.005 mol $ZrOCl_2$, 0.15 mol EG, and 0.005 mol I2959 were thoroughly mixed. The mixture was poured into a glass mold coated with a release film. The adaptive eutectic gel was cured under a nitrogen atmosphere in UV light (365 nm, 30 W) for 15 min to achieve final shaping.

Material characterization

^{1}H NMR spectra were acquired on a Bruker Avance 600 MHz spectrometer. The light transmittance of the eutectogels (thickness of 1 mm) was evaluated using a UV-Vis spectrophotometer (Shimadzu UV 3600) over the 800-400 nm range. Fourier-transform infrared (FTIR) spectra were collected in the attenuated total reflectance (ATR) mode on a Nicolet iS50 spectrometer, with a scanning range of 4,000-525 cm^{-1} and a spectral resolution of 4 cm^{-1}. Temperature-variable FTIR measurements were performed using the Nicolet iS50 FTIR spectrometer operated in transmission mode. The samples were sealed between two ZnSe windows, and the temperature was increased from 20 to 100 °C at 5 °C·min^{-1}. Two-dimensional correlation spectroscopy (2DCOS) was conducted on the temperature-variable transmission IR spectra, ranging from 20 to 100 °C, employing the 2D Shige software (version 1.3, ©Shigeaki Morita, Kwansei Gakuin University, Japan, 2004-2005) for analysis. The generated contour maps were visualized using the OriginPro program (version 2025). In the 2DCOS spectra, positive intensities are indicated in red, and negative intensities in blue. Rheological measurements were performed on a HAAKE MARS 60 modular rheometer (Thermo Fisher Scientific) equipped with a temperature control system, using a 25 mm-diameter parallel plate. Stress relaxation curves were measured at 25 °C under 10% strain and maintained for 3,600 s. Temperature-dependent G′/G″ curves were recorded over the 25-100 °C range at a constant frequency (10 rad·s^{-1}) and heating rate (5 °C·min^{-1}). Tensile tests were conducted on a universal mechanical testing machine (QT-1196, Dongguan Gaotai Technology), under standard conditions. Low-field ^{1}H NMR tests were carried out on a VTMR20-010V-I NMR analyzer (Suzhou Niumag Analytical Instrument Corporation) at a magnet field strength of 0.5 T. Ionic conductivity was determined by impedance measurement using an electrochemical workstation (CHI660E). The contact impedance between the electrode and skin was measured using the CHI660E workstation, ranging from 0.1 Hz to 10 kHz with an applied voltage of 200 mV.

Simulation calculations

The density functional theory (DFT) calculations were performed using the ORCA package with the B3LYP functional and Grimme's D4 dispersion correction. The def2-TZVP basis set was employed for all atoms, applying the def2/J auxiliary basis set for Coulomb fitting and the RIJCOSX approximation for efficient exchange integrals. The geometry optimization and frequency calculations were conducted with very tight self-consistent field (SCF) convergence criteria. Solvent effects were treated using the SMD implicit solvation model, with solvent parameters chosen for ethylene glycol to mimic the polar solvation effects in a deep eutectic environment. It should be noted that this model addresses the polar screening effect of the ethylene glycol medium without explicitly accounting for the competing interactions of ionic species from choline chloride. Further analyses of the key complexes were conducted in combination with an explicit solvation model.

Simulation

In this study, the finite element method was employed to analyze the tensile deformation of three different structural types (the primary structure, kirigami structure, and hybrid structure) of strain-sensing gels. The parameters for the gel electrode material were as follows: Poisson's ratio = 0.4; density = 1.28×10^4 kg/m^3; elastic modulus = 608 kPa. In the substrate simulation experiment, the base material was modified PDMS (Poisson's = 0.49, density = 970 kg/m^3, and elastic modulus = 7,500 kPa). The 2D models were analyzed applying a plane strain assumption. In order to ensure an accurate capture of stress concentrations at the hinges, the geometry was discretized using quadratic triangular elements (Quadratic Lagrange). A physics-controlled fine mesh was implemented, resulting in 31,349 nodes and 62,004 triangular elements for the hybrid structure. Mesh convergence was verified to ensure that the results were independent of element size. The interface between different material phases was modeled using a continuity boundary condition (perfectly bonded). The x-axis negative direction end of the model was fixed, and the tensile displacement was added in the x-axis positive direction.

Integration of bimodal devices

A kirigami-patterned strain gel was laid flat on a plastic release liner, and three pre-defined apertures in the center were filled with sEMG sensing electrodes. A custom flexible printed circuit (FPC) electrode was then aligned so the elongated pads contacted the two end strips of the strain gel and the three dedicated pads contacted the exposed surfaces of the sEMG gels, followed by encapsulation with a high-modulus PDMS. After full curing, the laminate was peeled from the release liner, applied over the gastrocnemius on the posterior calf, and secured around the perimeter with medical tape.

Sustainability evaluation

System sustainability was evaluated by performing a quantitative power consumption estimation of the edge node during active bimodal sampling and encrypted User Datagram Protocol (UDP) transmission. The system draws an average current of approximately 32.5 mA, with the primary energy consumption associated with the wireless module (68%) rather than cryptographic operations. Applying this profile, a compact 500 mAh battery provides over 13 hours of continuous operation. When combined with a modular, swappable battery design, the system demonstrates high practical viability for daily gait monitoring without necessitating heavy on-device inference.

Gait data collection protocol

Five healthy participants (aged 24.0 ± 2.4 years) were recruited to perform gait trials under a strictly standardized laboratory protocol. Data for each subject were collected across three separate sessions on different days, incorporating realistic inter-session variability, such as differences in sensor re-attachment and physiological fluctuations. This resulted in approximately 100 complete gait cycles per

participant (over 500 total segments). The experiments were conducted on a level, indoor flat surface with a total walking path length of 240 cm. Participants performed shuttle walking at a constant speed (0.4 m/s), which was synchronized using an audible metronome to minimize velocity-induced signal variance. The stride length was controlled at approximately 20 cm per step to ensure spatial uniformity. All the participants wore flat-soled athletic sneakers to minimize mechanical variables associated with the ground interface. The laboratory environment was regulated by a centralized air conditioning system, maintaining a stable ambient temperature of 24 ± 1 °C, ensuring consistent electrical and mechanical performance. Furthermore, each subject underwent a 5-minute habituation period to stabilize their gait pattern prior to formal recording.

Dataset preparation and segmentation

The identity recognition system was evaluated using a dataset collected from n = 5 healthy subjects comprising three males and two females: average age = 24.0 ± 2.4 years; height = 172.0 ± 4.7 cm; weight = 68.0 ± 6.8 kg. Details regarding demographic profiles are provided in Supplementary Table 1. Each participant performed 100 standardized gait cycles, providing a raw pool of 500 bimodal sensing sequences (comprising sEMG and Strain signals). A sliding window segmentation protocol was implemented to capture fine-grained temporal gait features and expand the sample size for deep learning. Taking a window size of 200 ms and an overlap of 50%, more than 8,000 gait sample segments were extracted and utilized for model training and validation.

Deep learning for the identity recognition system

The ByteEmbedded-TCN model was implemented in Python using PyTorch to classify AES-128 encrypted time-series without decryption. Each ciphertext sample was treated as a byte sequence (0-255). We first mapped bytes using a learnable 256×64 embedding table, then added a sinusoidal positional encoding to preserve temporal order. The embedded sequence was processed by a temporal convolutional network (TCN) composed of residual 1-D dilated convolutions (channels [16, 16, 32], kernel size 3, BatchNorm, Dropout = 0.2). A global average pooling layer aggregated features across time, followed by a fully connected classifier. We used stratified 5-fold cross-validation. Data loaders fed batches of 32 sequences where the models were trained for 100 epochs with Adam (initial learning rate 1e-2, no weight decay). We adopted Focal Loss ($\gamma = 2$, $\alpha = 0.25$) to deal with a potential class imbalance and focus learning on hard examples. A ReduceLROnPlateau scheduler monitored validation loss and reduced the learning rate by 0.5 after 15 stagnant epochs. We selected and check-pointed the weights with the highest validation accuracy. Performance was assessed on held-out folds via accuracy, confusion matrices, and t-SNE visualization of the logits to evaluate class separability. In practice, the combination of byte embedding + positional encoding + TCN yielded high accuracy with efficient inference, while preserving data privacy where the signal was never decrypted.

Statistical analysis

Data are expressed as the mean ± standard deviation (SD). All experiments were performed at least three times ($n \geq 3$) for each sample. The data were normalized when measuring the sEMG-strain gel signals and pre-processing training data. The statistical analysis was treated using Origin software.

Volunteer tests

This research adhered to local ethical standards and involved only non-invasive monitoring without risk to the participants or collection of sensitive data. Consequently, the study was exempt from formal ethical review. All the participants provided informed consent, and as co-authors of this study, they were fully aware of the experimental procedures and data usage.

RESULTS AND DISCUSSION

Wearable bimodal sensing system for ciphertext-domain gait recognition

The surface electromyography (sEMG) signals originate from descending motor commands transmitted via α-motoneurons to depolarize muscle fiber membranes. This process is accompanied by Ca^{2+} influx and actin-myosin sliding that drives muscle contraction and generates macroscopic deformation [Figure 1A]. Consequently, the electrophysiological activity and mechanical strain are strictly synchronized within the same motor unit, enabling sEMG and strain signals to complementarily represent the neuromuscular dynamics of gait [Figure 1Bi]. Applying this principle, we propose a privacy-preserving gait recognition strategy where high-fidelity inputs from the bimodal sensing units are locally encrypted and obfuscated utilizing the AES-128 algorithm [Figure 1Bii]. The encrypted signals are subsequently processed in the ciphertext domain using the ByteEmbedded-TCN, which performs temporal representation and classification without decryption [Figure 1Biii], enabling accurate identity authentication [Figure 1Biv]. The device can be worn unobtrusively and non-invasively on the gastrocnemius muscle [Supplementary Figure 2]. The kirigami structure is designed to enhance strain accommodation, and an additional enhancement layer with a modulus mismatch induces strain concentration, resulting in an amplified strain response [Figure 1C]. The high performance of each sensing modality, combined with the inherent complementarity, is key to maintaining a high recognition accuracy under encrypted conditions.

In the case of the strain sensing channel, the hierarchical supramolecular aggregates are based on UPy units, involving multiple hydrogen bonds and dynamic π-π stacking interactions[22]. The multiple hydrogen bonds endow the network with a stable reversible cross-linking and high load-bearing capacity, whereas the π-π stacking promotes a reversible depolymerization and reassembly of the aggregates during cyclic deformation. The associated synergism effectively disperses stress and inhibits irreversible energy dissipation, where the eutectogel exhibits low hysteresis, low baseline drift, and enhanced long-term dynamic tracking stability under cyclic loading [Figure 1D]. The design of the sEMG sensing channel is based on a previously reported dynamically adaptive eutectogel network[23]. This configuration mitigates strain-induced interference of electromyographic signals while preserving high interfacial compliance, enabling a high-fidelity, low-noise recording [Figure 1E]. The synergy of the two modalities enhances feature entropy and temporal resolution and confers robustness and scalability to gait recognition in encrypted environments.

Structure and characterization of $PMDU_3$ eutectogels

We have developed a hierarchical supramolecular eutectogel network based on UPy-mediated multiple hydrogen bonding and π-π stacking interactions [Figure 2A]. In contrast to conventional deep eutectic solvent (DES)-based gels, which can be dominated by viscous dissipation due to the intrinsically high viscosity of DES[24], the proposed design introduces robust yet reversible physical cross-linking domains. The hierarchical aggregates enable efficient load transfer under deformation while facilitating rapid structural reconstruction upon unloading, reducing energy dissipation and suppressing hysteresis.

Applying this design concept, eutectogel system fabrication involved a one-step *in situ* UV-initiated copolymerization. The UPy-HBA monomer bearing polymerizable double bonds was synthesized in accordance with a reported method[20,21], and the chemical structure was confirmed by ^{1}H NMR spectroscopy. Methacrylic acid (MAA) and [2-(methacryloyloxy)ethyl]dimethyl-(3-sulfopropyl)ammonium hydroxide (DMAPS) were employed as comonomers, UPy-HBA served as the supramolecular cross-linker, and ethylene glycol (EG)/choline chloride (ChCl) was used as the deep eutectic solvent. The absence of a C=C stretching vibration at 1,654 cm^{-1} in the FT-IR spectrum confirms successful polymerization [Supplementary Figure 3][25]. The resulting eutectogel exhibited an optical transmittance of up to 92.3% [Supplementary Figure 4], suggesting no obvious macroscopic phase separation and providing a structural basis for uniform stress transfer[26].

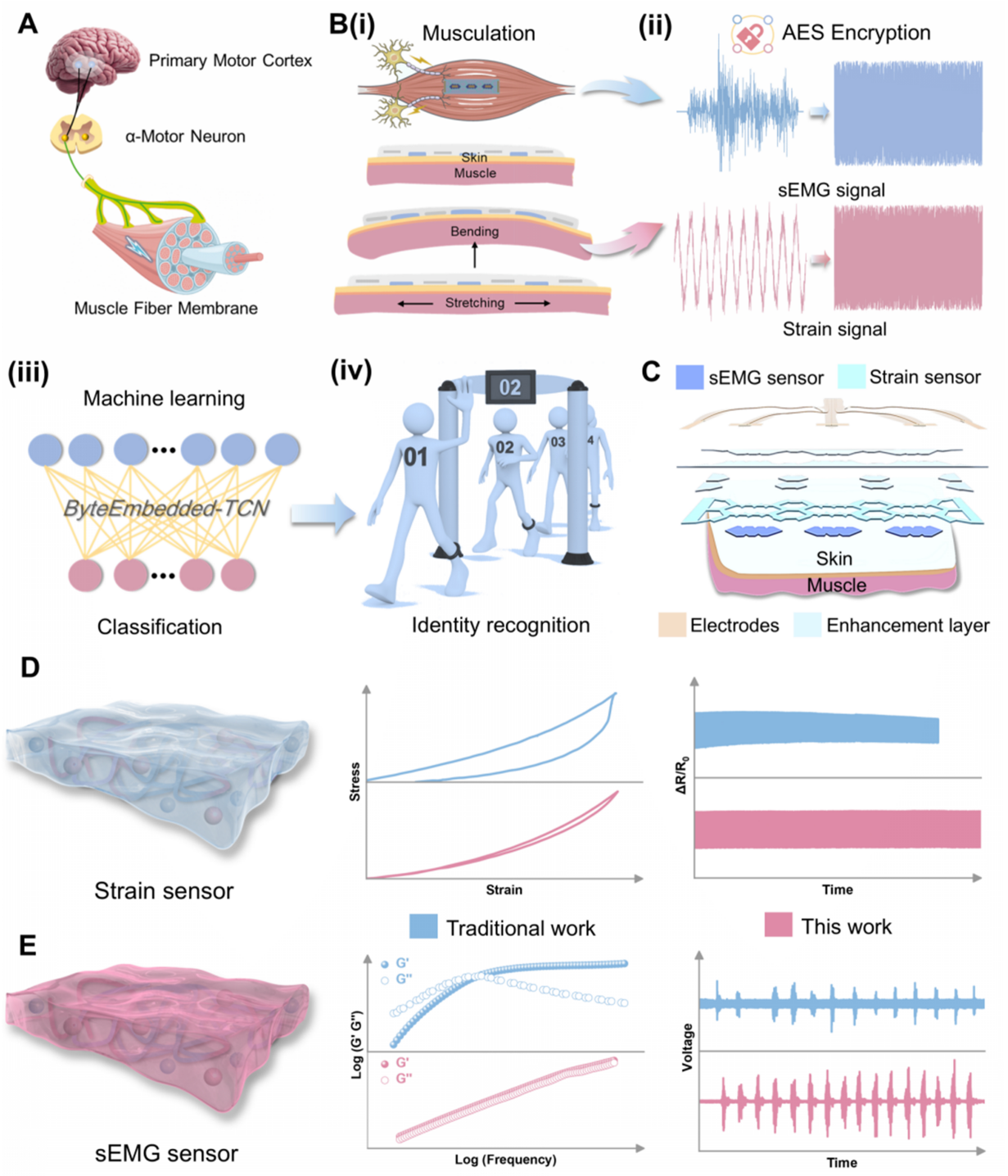

Figure 1. (A) Mechanism of sEMG signal generation; (B) Identity recognition with privacy protection based on mechanical and bioelectrical signals; (C) Expanded schematic representations of the device; (D) and (E) Schematic representations of the differences between the proposed gels and conventional gels in terms of mechanical and electrical properties. Note: the curves represent qualitative schematics intended to show performance trends. sEMG: Surface electromyography; AES: Advanced Encryption Standard; ByteEmbedded-TCN: ByteEmbedded Temporal Convolutional Network.

In order to establish the optimal composition of the supramolecular network, eutectogels with different UPy-HBA contents ($PMDU_x$, x = 0-4) were systematically investigated. Tensile tests have shown that the Young's modulus and fracture strength increase monotonically with increasing UPy-HBA content [Figure 2B], indicating an enhanced load-bearing capability due to the higher density of supramolecular aggregates

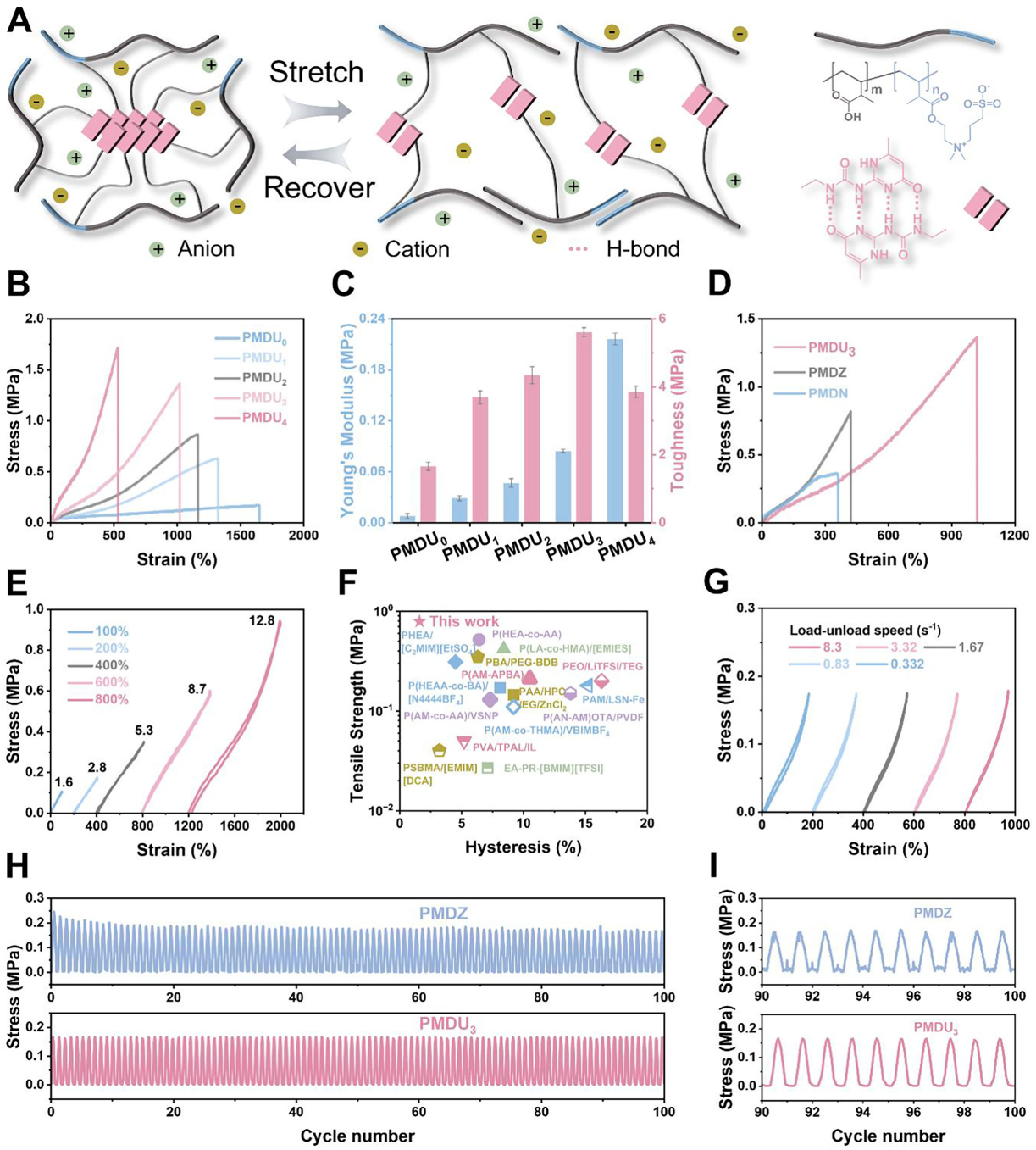

Figure 2. (A) Schematic representation illustrating the mechanism associated with enhanced eutectogel toughness and low-hysteresis, where the hierarchical aggregates self-assemble via quadruple hydrogen bonds and π-π stacking acts as cross-linkers; (B) Stress-strain curves for $PMDU_{0-4}$ eutectogels; (C) The Young's modulus and toughness of $PMDU_{0-4}$ eutectogels; (D) Stress-strain curves for PMDN, PMDZ, and $PMDU_3$ eutectogels; (E) Cyclic tensile testing curves for $PMDU_3$ eutectogel at different strains; (F) Comparison of the hysteresis values and breaking strength of the $PMDU_3$ eutectogel and other reported low-hysteresis gels; (G) Cyclic tensile testing curves for $PMDU_3$ eutectogel at different strain rates; (H) Cyclic loading-unloading curves for PMDZ and $PMDU_3$ eutectogels over 100 cycles at 200% strain; (I) Expanded view of the last 10 cyclic loading-unloading curves. Note: data are shown as mean ± SD for $n = 3$ independent samples. PMDU: UPy-crosslinked poly (methacrylic acid-co-DMAPS) network; PMDN: covalently crosslinked poly (methacrylic acid-co-DMAPS) network; PMDZ: Zr^{4+}-coordinated poly (methacrylic acid-co-DMAPS) network; SD: standard deviation; PHEA: poly(2-hydroxyethyl acrylate); HEA: 2-hydroxyethyl acrylate; AA: acrylic acid; HEAA: 2-hydroxyethyl acrylate; BA: butyl acrylate; AM: acrylamide; APBA: 3-acrylamidophenylboronic acid; VSNP: vanadium sesquioxide nanosheets; THMA: 2,3,4,5-tetrahydroxybenzaldehyde methacrylate; AN: acrylonitrile; OTA: oxalic acid; PVDF: polyvinylidene fluoride; LA: lactic acid; HMA: hydroxymethyl acrylate; [EMIES]: 1-ethyl-3-methylimidazolium ethylsulfate; PBA: poly(butyl acrylate); PEG: polyethylene glycol; BDB: 1,4-butanediol; PAA: poly(acrylic acid); HPC: hydroxypropyl cellulose; EG: ethylene glycol; PVA: poly(vinyl alcohol); TPAL: tripropylene glycol monoacrylate; IL: ionic liquid; PSBMA: poly(sodium 4-styrenesulfonate); EA: ethyl acrylate; PR: phenolic resin; [BMIM][TFSI]: 1-butyl-3-methylimidazolium bis(trifluoromethylsulfonyl)imide; PEO: poly(ethylene oxide); LiTFSI: lithium bis(trifluoromethylsulfonyl)imide; ITEG: isotetraglyme; LSN: layered double hydroxide.

formed by multiple hydrogen bonds and π-π stacking interactions[27]. In contrast, sample toughness exhibits a non-monotonic trend and reaches a maximum at 3 mol% UPy-HBA [Figure 2C]. This suggests that moderate supramolecular cross-linking can reinforce the network and enable stress dissipation through reversible structural rearrangement, whereas excessive cross-linking restricts chain mobility and results in brittle fracture. The advantage of the hierarchical supramolecular network was further demonstrated by preparing a covalently cross-linked gel (PMDN) and a metal ion cross-linked gel (PMDZ) as control systems [Figure 2D and Supplementary Figure 5]. The PMDN exhibits the lowest fracture strength and elongation, which is attributed to the permanently fixed cross-linking sites that cannot dissipate stress. The PMDZ shows improved mechanical properties due to reversible coordination interactions, but is limited by the relatively slow rearrangement dynamics[28]. In contrast, $PMDU_3$ achieves the best balance of strength and ductility, confirming that the hierarchical supramolecular aggregates enable efficient energy dissipation while maintaining structural integrity.

Cyclic loading-unloading tests have established the occurrence of an optimal supramolecular cross-linking window [Supplementary Figure 6]. The hysteresis ratio decreases and subsequently increases with increasing UPy-HBA content, reaching a minimum at 3 mol%. At a low UPy-HBA content, insufficient supramolecular constraints lead to disordered chain slippage and amplified viscous dissipation in the high-viscosity DES environment, whereas excessive cross-linking suppresses chain mobility and prevents effective stress release. Taking mechanical robustness and energy dissipation into account, $PMDU_3$ was selected as the optimal composition. As shown in Figure 2E, $PMDU_3$ maintains a low hysteresis ratio (< 15%) even at 800% strain, outperforming most reported supramolecular gels [Figure 2F and Supplementary Table 2]. Moreover, the hysteresis response shows a negligible strain-rate dependence [Figure 2G], suggesting a fast reversible reconstruction of the supramolecular network[29]. Long-term cyclic tests have demonstrated a high degree of mechanical stability: $PMDU_3$ exhibits almost no stress decay over 100 cycles, whereas PMDZ shows significant attenuation [Figure 2H and I].We subjected the $PMDU_3$ eutectogel to 10,000 consecutive loading-unloading cycles [Supplementary Figure 7] to establish that the low-hysteresis characteristics ensure stable performance in long-term operation. The results demonstrate no obvious stress attenuation following the cyclic tests. The hierarchical supramolecular cross-links enable efficient stress dissipation during deformation and rapid structural recovery after unloading.

In addition to tensile and cyclic performance, $PMDU_3$ also exhibits improved notch resistance and a self-healing capability [Supplementary Figures 8 and 9]. The notch-resistant response serves to indicate that the hierarchical supramolecular network can effectively dissipate local stress at crack tips and inhibit crack propagation, increasing damage tolerance and maintaining structural integrity under practical operating conditions[30]. The self-healing behavior further confirms the dynamic reversibility of the supramolecular cross-links and associated multiple hydrogen bonds and π-π stacking, which allows structural reconstruction and functional recovery after damage. In addition, $PMDU_3$ exhibits robust adhesion to a variety of substrates [Supplementary Figure 10], consistent with a high degree of interfacial compatibility. This adhesion is beneficial in maintaining stable interfacial contact and reducing strain transmission loss and signal fluctuation caused by interfacial slippage. These results demonstrate that the hierarchical supramolecular cross-linking strategy enables high strength and toughness with low hysteresis, significantly improving the damage tolerance, interfacial stability, and long-term dynamic reliability of the eutectogel.

Mechanistic analysis of low hysteresis properties in $PMDU_3$ eutectogels

The molecular origin of the low-hysteresis behavior in the $PMDU_3$ eutectogel was addressed by investigating the relative strengths of the supramolecular interactions in the network using density functional theory (DFT) calculations [Figure 3A]. The calculated binding energies reveal a clear hierarchy with respect to the intermolecular interactions. The multiple hydrogen bonds formed between the UPy-HBA units possess the

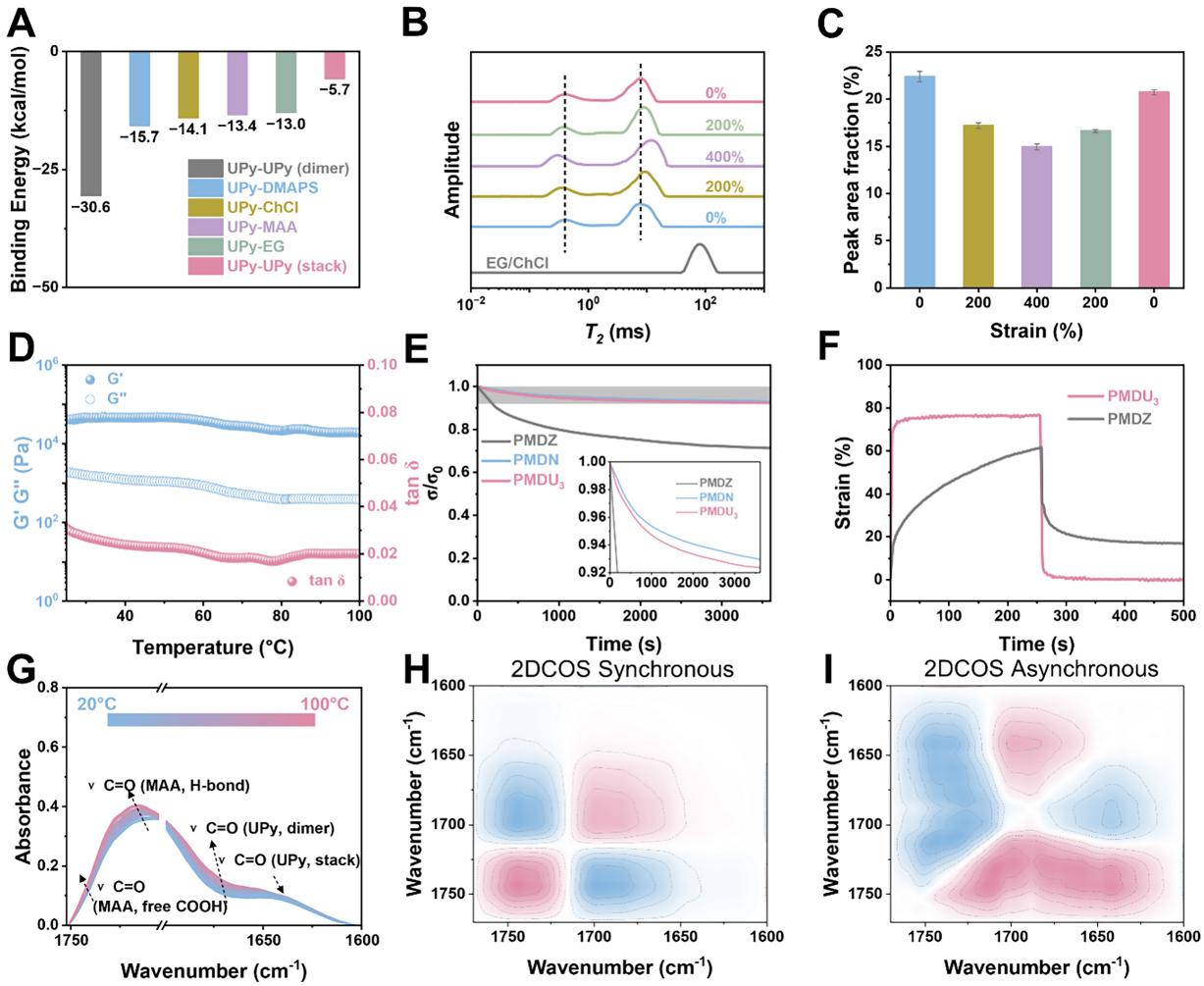

Figure 3. (A) Binding energy of UPy-HBA with different components; (B) Low-field ^{1}H NMR results for PMDU$_3$ eutectogel under *in situ* stretching; (C) Variation of the peak area fraction for ν(C=O) in UPy-HBA under *in situ* stretching as a function of strain; (D) Temperature ramp curves for the PMDU$_3$ eutectogel from 25 to 100 °C at a heating/cooling rate of 5 °C·min^{-1}; (E) Stress relaxation curves for PMDN, PMDZ, and PMDU$_3$ eutectogels recorded at 25 °C with 10% strain; (F) Creep recovery curves for PMDZ and PMDU$_3$ eutectogels measured at 25 °C under a constant stress of 100 kPa; (G) Temperature-variable FTIR spectra of PMDU$_3$ eutectogel following thermal treatment from 20 to 100 °C (interval: 5 °C); (H) and (I) 2DCOS synchronous and asynchronous spectra respectively generated from (G). Note: in the 2DCOS spectra, red colors represent positive intensities and blue colors represent negative intensities. Data are shown as mean ± SD for n = 3 independent samples. UPy-HBA: 4-{6-[3-(6-Methyl-4-oxo-1,4-dihydropyrimidin-2yl)ureido]hexyl carbamoyloxy}butyl acrylate; NMR: nuclear magnetic resonance; PMDU: UPy-crosslinked poly (methacrylic acid-co-DMAPS) network; PMDN: covalently crosslinked poly (methacrylic acid-co-DMAPS) network; PMDZ: Zr^{4+}-coordinated poly (methacrylic acid-co-DMAPS) network; 2DCOS: two-dimensional correlation infrared spectroscopy; SD: standard deviation; DMAPS: *N*-(3-sulfopropyl)-*N*-(methacryloxyethyl)-*N*,*N*-dimethylammonium betaine; ChCl: choline chloride; MAA: methacrylic acid; EG: ethylene glycol.

highest binding energy, followed by interactions between UPy-HBA and the polymer chains derived from MAA/DMAPS, whereas the π-π stacking interactions exhibit comparatively lower binding energies[31]. These results indicate that the network supramolecular interactions are not energetically equivalent but contribute to a hierarchical interaction system. In this configuration, the strong hydrogen-bonding motifs provide the primary load-bearing framework, and the weaker π-π stacking interactions act as dynamic interaction sites that are more responsive to external perturbations.

The response of the supramolecular interactions to mechanical deformation has been assessed experimentally by *in situ* tensile low-field nuclear magnetic resonance measurements [Figure 3B]. As the applied strain is increased, the T_2 relaxation time associated with polymer-chain protons shows a gradual

decrease, indicating reduced segmental mobility and enhanced local constraints as the network chains are progressively oriented during stretching[32]. In contrast, the T_2 relaxation time of the solvent molecules increases with strain, suggesting that the local microenvironment surrounding the supramolecular aggregates is temporarily loosened, facilitating solvent mobility. When the strain is returned to zero, both relaxation times recover to values close to their original states. This reversibility indicates that the deformation involves dynamic rearrangement of the supramolecular structures rather than irreversible damage to the polymer network. Further evidence for the dynamic nature of the supramolecular interactions was obtained by *in situ* infrared spectroscopy during tensile deformation [Figure 3C and Supplementary Figure 11]. As the strain is increased, the peak area associated with the ν(C=O) vibration of UPy-HBA decreases, indicating partial dissociation or rearrangement of the supramolecular interactions during stretching. Upon releasing the strain, the corresponding spectral features recover to approach their initial states. This reversible spectral evolution confirms that the supramolecular cross-linking domains undergo dynamic dissociation and reassembly under mechanical loading, which enables the network to accommodate deformation while preserving structural integrity.

The macroscopic viscoelastic behavior of the network was evaluated in temperature-dependent rheological measurements [Figure 3D]. Over the 25-100 °C temperature range, the storage modulus (G′) and loss modulus (G″) are nearly constant with a loss factor (tan δ) of approximately 0.02. This temperature-insensitive viscoelastic response indicates that thermal perturbation does not significantly weaken the load-bearing capability of the network or induce additional viscous dissipation. This behavior contrasts with standard DES-based gels, where an increase in temperature accelerates segmental friction and relaxation[33]. The stable rheological response suggests that the supramolecular network possesses sufficient structural robustness to maintain its integrity under thermal stimulation.

We have compared the relaxation and recovery behavior of $PMDU_3$ with covalently cross-linked and metal-ion cross-linked systems. Stress relaxation measurements have shown that $PMDU_3$ exhibits a degree of stress retention comparable to that of the covalently cross-linked gel, whereas the metal-ion cross-linked network undergoes significantly faster stress decay [Figure 3E]. This observation indicates that the supramolecular network in $PMDU_3$ does not behave as a loosely organized dynamic system but retains a constrained structure capable of sustaining a mechanical load[34]. Creep-recovery experiments have established the difference in reversible reconstruction capability [Figure 3F]. After unloading, $PMDU_3$ rapidly returns to its initial state with minimal residual deformation, whereas the metal-ion cross-linked gel exhibits a pronounced permanent deformation. The metal coordination bonds can dissociate readily under stress, but the associated reformation rate is relatively low and is accompanied by irreversible structural rearrangements. In contrast, the supramolecular interactions in $PMDU_3$ facilitate rapid network reconstruction after unloading.

The thermal response of the supramolecular aggregates was also evaluated using variable-temperature FTIR spectroscopy [Figure 3G]. As the temperature is increased from 20 to 100 °C, the characteristic absorption bands associated with the stacked UPy-HBA aggregates show a gradual decrease in intensity, and the signals corresponding to free associative units increase. This spectral evolution is consistent with a progressive dissociation of the supramolecular aggregates in response to thermal perturbation, confirming the dynamic nature of the interaction network. A 2DCOS analysis was conducted [Figure 3H and I, and Supplementary Table 3]. According to Noda's rules[35], the thermal response sequence for the characteristic peaks (1,695 → 1,686 → 1,744 → 1,713 → 1,640 → 1,726 cm^{-1}) corresponds to the evolution of UPy dimers, free carboxyl groups from MAA, urethane groups from UPy-HBA, stacked UPy structures, and hydrogen-bonded complexes with the DES components. This asynchronous evolution indicates that different supramolecular motifs respond to external perturbations at different stages, reflecting the hierarchical organization of the interaction network.

The results indicate that the supramolecular network in $PMDU_3$ combines structural stability with dynamic reversibility. Strong hydrogen-bonded motifs stabilize the primary network framework, whereas weaker interactions can dynamically rearrange under external perturbations. This cooperative interaction hierarchy serves to accommodate deformation through reversible molecular rearrangement while maintaining mechanical integrity, suppressing hysteresis during cyclic loading.

Electrical characteristics of bioelectrical and mechanical sensors

The $PMDU_3$ eutectogel exhibited a high ionic conductivity of up to 5.4 $mS \cdot cm^{-1}$ [Supplementary Figure 12], which can be attributed to the high concentration of mobile ionic species present in the deep eutectic solvent, together with the enhanced ion transport pathways provided by the zwitterionic polymer network[36]. To further evaluate its electromechanical performance at the device level, the electrical response of the gel was systematically characterized under both static and dynamic mechanical deformation. As shown in Figure 4A, the gauge factor [$GF = \delta(\Delta R/R_0)/\delta S$] reached 0.77 within the 0%-200% strain range and increased to 2.50 over the 200%-500% strain range, demonstrating high sensitivity across a broad detection window. Notably, the $PMDU_3$ eutectogel, when employed as a strain-sensing element, exhibited enhanced sensitivity at moderate-to-high deformation levels (200%-500%). However, in most practical applications, the applied strain typically remains below 50%. To enhance the effective sensing range, a kirigami-inspired structural design was introduced to exploit the modulus mismatch between compliant and rigid layers, thereby enabling stress concentration and amplification of localized deformation. In this soft-hard hybrid architecture, the kirigami strain-sensing layer contains three centrally positioned apertures embedded with low-modulus sEMG eutectogel domains, while the surrounding regions are back-filled and encapsulated with high-modulus PDMS, creating a pronounced mechanical modulus contrast. Finite-element simulations of three structural configurations, namely the pristine, kirigami-only, and soft-hard hybrid architectures, subjected to 50% tensile strain [Figure 4B], revealed that interfacial stress concentration within the hybrid structure induces pronounced localized deformation of the gel domains. Simultaneously, the kirigami cuts transform in-plane tensile deformation into hinge-like out-of-plane opening motions, thereby enabling secondary mechanical amplification and reducing the force threshold required to induce deformation. Moreover, compared with the conventional architecture, the soft-hard hybrid design exhibited the greatest increase in maximum principal strain with increasing displacement across all simulated deformation conditions [Figure 4C]. As shown in Figure 4D, the relative resistance variation increased monotonically and reproducibly over a wide strain range of 10%-500%, while the highly overlapped loading curves and stable baseline response further confirmed the excellent measurement reliability and sensing precision of the device. During cyclic fatigue testing, the commercial gel-based sensor exhibited baseline drifts exceeding 15% after 1,000 loading-unloading cycles [Supplementary Figure 13]. In contrast, the developed eutectogel sensor maintained excellent signal stability, with a baseline drift of less than 1% even after 10,000 cycles [Figure 4E].

Moreover, to rigorously assess the mechanical robustness of the sEMG interface, signal stability was systematically evaluated under vigorous vibrational conditions. As shown in Figure 4F, the signals acquired using the commercial gel electrode were initially stable. However, upon exposure to intense vibration (4 $rad \cdot s^{-1}$), substantial noise artifacts rapidly developed, causing severe signal distortion and ultimately rendering the acquired signals indistinguishable from background noise, resulting in signal acquisition failure. In contrast, the developed eutectogel electrode maintained stable sEMG waveforms under identical testing conditions, exhibiting negligible noise amplification and preserving a high signal-to-noise ratio (~40 dB). These findings highlight the outstanding mechanical robustness and interfacial stability of the electrode under dynamic mechanical perturbation. Furthermore, short-time Fourier Transform (STFT)-based frequency-domain analysis validated these observations, revealing substantially lower motion-induced spectral noise than that of the commercial reference gel electrode [Figure 4G]. Following the integration of the two sensing eutectogels, a wearable gait-based identity recognition system was successfully developed. As

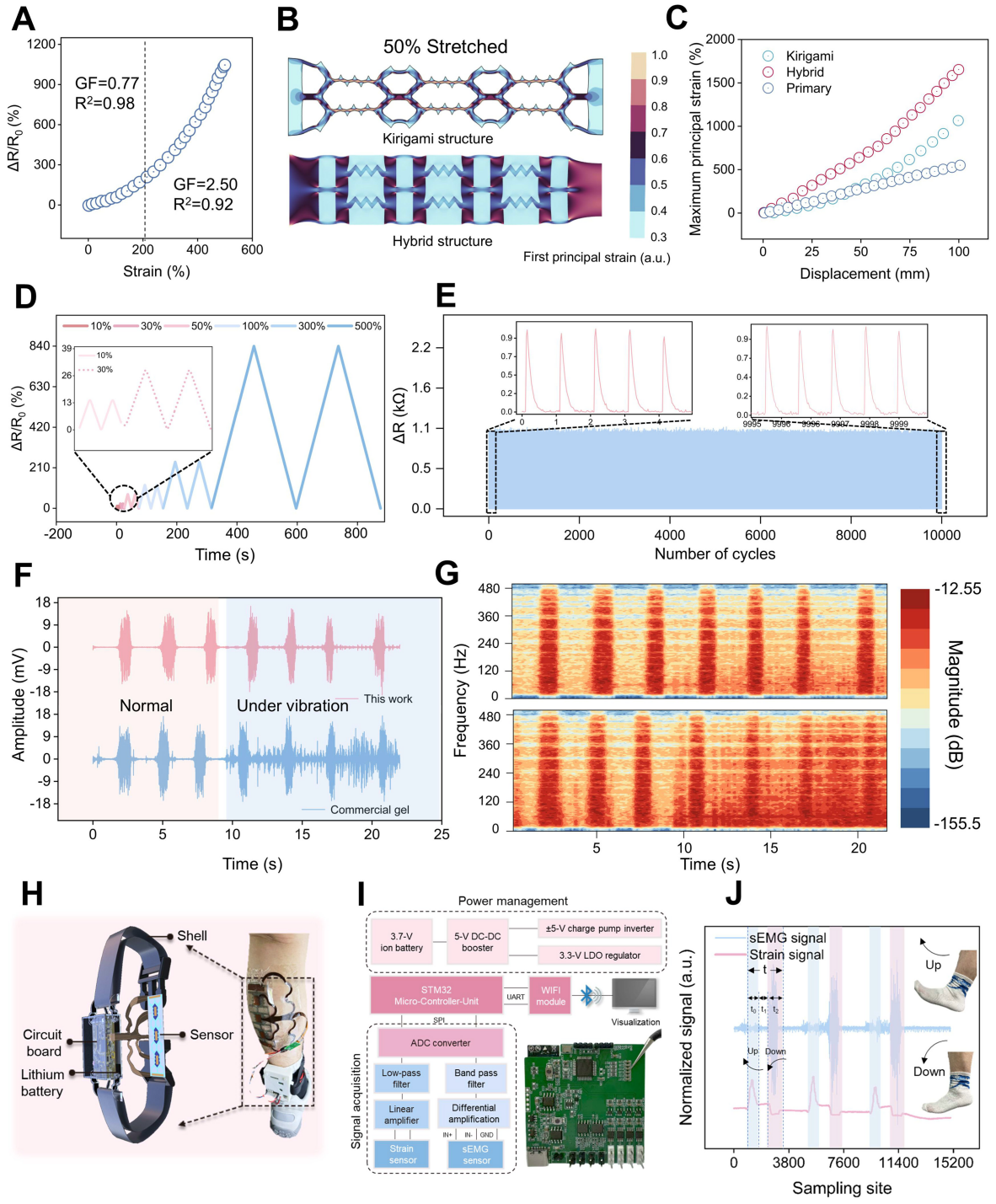

Figure 4. (A) Determination of the sensor gauge factor (GF); (B and C) Finite element simulation analysis of the principal strain distributions in the proposed pristine, kirigami, and soft-hard hybrid structure; (D) Dynamic sensing response of the strain sensor under varying tensile strains ranging from 10% to 500%; (E) Long-term cyclic stability evaluation over 10,000 loading-unloading cycles; (F) Time-domain sEMG signals recorded using the developed eutectogel electrode and a commercial gel electrode under both static and vibration conditions; (G) Corresponding short-time Fourier transform (STFT) spectrograms of the sEMG signals obtained under static and vibration states; (H) Exploded schematic illustration and photographic image of the wearable sensing systems; (I) Schematic representation of the integrated circuitry and overall system workflow; (J) Normalized bimodal sensing signals recorded during gait-related movements. sEMG: Surface electromyography; R^2: coefficient of determination; DC: direct current; LDO: low dropout regulator; STM32: STMicroelectronics 32-bit microcontroller; UART: universal asynchronous receiver/transmitter; WIFI: wireless fidelity; ADC: analog-to-digital converter.

illustrated in the exploded schematic shown in Figure 4H, the sensors were positioned over the gastrocnemius muscle and secured using medical-grade adhesive tape. The acquired signals were transmitted through a carefully engineered flexible printed circuit (FPC) electrode to the signal-acquisition electronics, which were encapsulated within a custom-designed 3D-printed housing and mounted around the ankle using an adjustable strap to ensure stable mechanical contact during motion. The hardware architecture of the acquisition unit [Figure 4I] comprises signal-conditioning, power-management, and wireless transmission modules. By integrating a high-speed analog-to-digital converter (ADC), a Serial Peripheral Interface (SPI)-based communication link, and a User Datagram Protocol (UDP)-based wireless transmission protocol, the system achieves an integrated eight-channel configuration with a sampling rate of 1 K/s, enabling reliable, high-fidelity acquisition of gait signals for identity recognition applications. Figure 4J illustrates the complementary sensing capabilities of the developed dual-modal sensing platform for gait monitoring. The sEMG eutectogel and $PMDU_3$ eutectogel sensing units were arranged in a coplanar configuration to minimize spatiotemporal mismatch during signal acquisition. A normalized gait cycle was characterized by three representative phases: dorsiflexion (t0), the inter-phase transition interval (t1), and plantarflexion (t2), corresponding to muscle activation rate, contraction amplitude, and phase dwell time, respectively. Empirically, the sEMG eutectogel exhibited pronounced signal responses during plantarflexion, corresponding to active contraction of the gastrocnemius muscle, whereas comparatively weaker signals were observed during dorsiflexion, which is primarily associated with passive muscle elongation. In contrast, the $PMDU_3$ eutectogel provided complementary mechanotransductive sensing behavior. Specifically, dorsiflexion induced outward bulging of the posterior calf region, generating tensile deformation within the sensor and consequently increasing its electrical resistance. Conversely, plantarflexion produced a concave deformation profile, imposing compressive strain on the sensor and decreasing resistance. Unlike most commercial strain gauges, which predominantly exhibit unidirectional sensing characteristics [Supplementary Figure 14], the developed eutectogel sensor demonstrated bidirectional responsiveness to both tensile and compressive deformation, thereby significantly enhancing sensing observability. Furthermore, the bimodal sensing strategy effectively compensated for the relatively weaker compressive response, yielding more comprehensive and reliable motion characterization. In the frequency domain, STFT analysis revealed distinct motor-unit firing frequency bands, along with vibration-associated spectral components arising from tendon and skin deformation, thereby providing a quantitative representation of dynamic movement behavior [Supplementary Figure 15].

AI-enabled encrypted gait-based identity recognition

To ensure the secure transmission of data to downstream servers, the acquired signal streams were encrypted using the AES-128 algorithm[37] [Figure 5A]. AES-128 employs a 128-bit encryption key and 10 iterative transformation rounds, providing a sufficiently large key space (2^{128}) that renders brute-force attacks computationally impractical, requiring approximately 1.1×10^{13} years at 10^{18} guesses/s. Although the encryption process effectively obscures the amplitude and temporal characteristics of the sEMG and strain signal exemplars from direct visual interpretation [Figure 5B and C], the intrinsic integrity of the underlying data remains fully preserved. Correlation analysis between the original and decrypted signals yielded an R^2 = 1.000 and an RMSE = 0.000, thereby confirming the complete numerical fidelity of the transmission pipeline and the bitwise lossless nature of the decryption process [Supplementary Figure 16].

The proposed end-to-end encrypted gait-based identity recognition pipeline [Figure 5D] transforms encrypted bimodal sensing streams into byte-level sequences, then normalizes, removes noise, and performs block-wise preprocessing, including segmentation, filtering, and padding, to generate inputs suitable for machine learning analysis. The core ByteEmbedded-TCN framework [Figure 5E] is built upon a TCN architecture comprising causal and dilated one-dimensional convolutional layers integrated with residual blocks, thereby enabling a large effective receptive field while maintaining fixed processing latency. Owing to

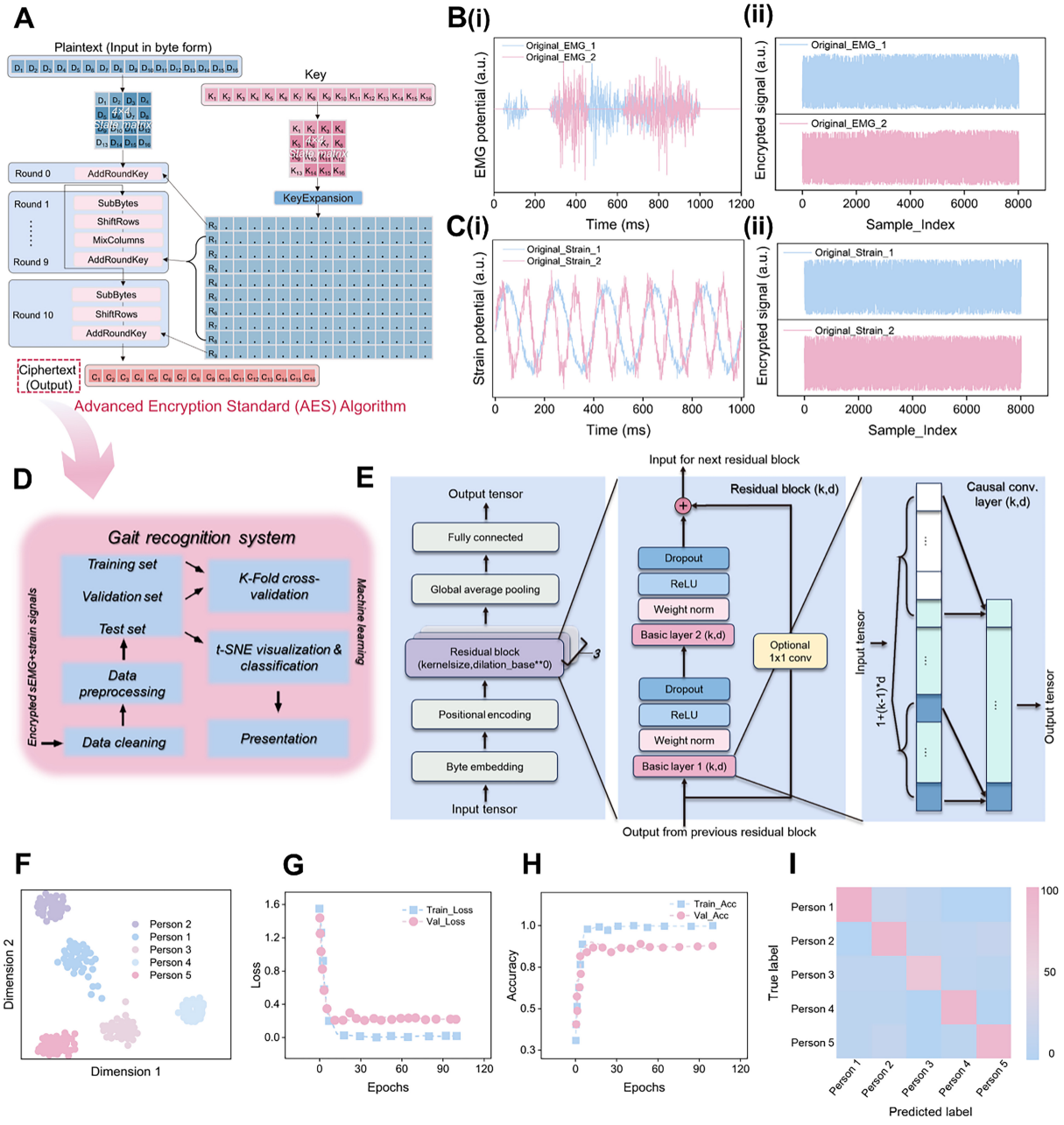

Figure 5. (A) Schematic flowchart of the AES-128 encryption algorithm; (B) Representative sEMG signal waveforms before and after encryption; (C) Representative strain-sensing signal waveforms before and after encryption; (D) Software workflow of the gait-based identity recognition system; (E) Architecture of the proposed ByteEmbedded-TCN model; (F) t-distributed stochastic neighbor embedding (t-SNE) visualization of identity recognition clustering results; (G) Training and validation loss curves of the neural network model; (H) Training and validation accuracy curves of the neural network model; (I) Confusion matrix illustrating the recognition performance of the proposed system. AES-128: Advanced Encryption Standard-128; sEMG: Surface electromyography; ByteEmbedded-TCN: ByteEmbedded Temporal Convolutional Network; EMG: electromyography; Train_Acc: training accuracy; Val_Acc: validation accuracy.

the inherent parallelism of convolutional operations, the model exhibits low training and inference latency, as well as enhanced robustness against temporal jitter and minor sampling-rate fluctuations. For encrypted ciphertext inputs, the conventional sparse one-hot encoding was replaced with learnable byte embeddings spanning the range 0-255, enabling the model to effectively capture statistical co-occurrence relationships among encrypted byte patterns and fragments.

To further enhance sequence representation, positional encoding was incorporated to encode both absolute packet positions and relative positional indices modulo 16 within AES blocks. This design aligns well with the block independence and deterministic properties of ECB-mode encryption, thereby enabling the model to effectively exploit stable structural features, including repeated ciphertext blocks and block-boundary patterns. When evaluated on randomly mixed datasets using stratified five-fold cross-validation, the learned feature representations demonstrated distinct inter-class separability in the t-distributed stochastic neighbor embedding (*t*-SNE) space [Figure 5F]. After 100 training epochs, the proposed model achieved a classification accuracy of 89.7% ± 1.2%, with stable convergence throughout training [Figure 5G and H]. In comparison, evaluation using plaintext data yielded a baseline accuracy of 95.1% ± 0.8%, together with consistent loss reduction during training [Supplementary Figure 17], indicating that the encrypted framework incurs only an acceptable 5.4% performance reduction while preserving data privacy. Furthermore, the confusion matrix demonstrates robust overall identity recognition performance across different subjects [Figure 5I]. To further evaluate the long-term generalizability of the proposed framework, an independent cross-session validation test was conducted approximately 80 days later. Using the originally pre-trained model to infer 28,000 gait segments corresponding to 80 cycles per subject, the system consistently maintained a high average classification accuracy of 86.5%, thereby demonstrating strong temporal robustness and stability of the learned identity representations. The detailed recognition outcomes and fine-grained evaluation metrics, including precision, recall, and F1-score, for the longitudinal cross-session assessment are summarized in the corresponding confusion matrix [Supplementary Figure 18] and performance metric table [Supplementary Table 4], respectively. Furthermore, channel-width ablation analysis revealed that classification accuracy was sensitive to the number of residual output channels in the network architecture [Supplementary Figure 19A], while incorporating byte-embedding consistently improved model performance relative to conventional encoding strategies [Supplementary Figure 19B]. Compared with conventional CNN, LSTM, and Transformer-based baseline models, the proposed ByteEmbedded-TCN architecture demonstrated substantially superior performance in encrypted signal classification tasks [Supplementary Figure 19C]. To further assess the effectiveness and computational efficiency of the proposed framework, a comprehensive model-complexity analysis was conducted, with the results summarized in Supplementary Table 5. The results demonstrate that the proposed ByteEmbedded-TCN architecture achieves superior recognition performance while maintaining an extremely lightweight model complexity, comprising only 12.02 k trainable parameters and 4.91 M floating-point operations (FLOPs). This computational efficiency is significantly greater than that of high-capacity architectures such as Transformer-based models. Furthermore, as a baseline comparison, classifiers utilizing only a single sensing modality failed to achieve classification accuracies exceeding 80% [Supplementary Figure 20], thereby confirming the distinct performance advantage of the proposed bimodal sensing framework.

Finally, implementing AES-128 in in Electronic Codebook (ECB) mode within the proposed privacy-preserving framework entails certain trade-offs. Although this deterministic encryption strategy enables computationally efficient ciphertext-domain inference on resource-constrained hardware platforms, it may still expose certain global statistical properties of gait patterns to potential adversaries. ECB mode was selected to preserve deterministic block-level consistency required for efficient ciphertext-domain feature extraction on low-power wearable hardware. This approach can therefore be regarded as a task-oriented encryption strategy that prioritizes the concealment of raw physiological signal magnitudes rather than maximizing absolute cryptographic entropy. Future investigations will focus on integrating differential privacy mechanisms or randomized noise-injection layers to reduce potential statistical information leakage further while preserving high identity recognition accuracy. Furthermore, to achieve the level of imperceptible wearability required for long-term continuous monitoring, future integration of the developed gel materials with advanced microfabrication technologies may enable substantial device miniaturization and enhanced user comfort.

CONCLUSIONS

In this study, a privacy-preserving gait recognition framework integrating multimodal wearable sensing with ciphertext-domain machine learning was established. A dual-mode strain and surface electromyography (sEMG) sensing platform was engineered to acquire mechanical and bioelectrical gait signals simultaneously. The strain-sensing component was constructed using a supramolecular eutectogel reinforced by UPy-HBA-mediated multiple hydrogen-bonding interactions and π-π stacking, enabling ultralow hysteresis (1.6% at 100% strain) while maintaining excellent mechanical elasticity and long-term operational stability over 10,000 deformation cycles. In parallel, the adaptive eutectogel-based sEMG electrode exhibited high interfacial compliance and stable skin adhesion, thereby enabling reliable acquisition of myoelectric signals with a signal-to-noise ratio exceeding 40 dB while effectively suppressing motion-induced artifacts during dynamic movements. Building upon this sensing platform, a ciphertext-domain recognition framework was subsequently established, in which multimodal physiological signals were locally encrypted using AES-128 and directly processed through a ByteEmbedded-TCN architecture. Benefiting from causal convolutional operations that preserve temporal dependencies, together with embedded feature representations that enable efficient parsing of encrypted sequences, the proposed model achieved a gait identification accuracy of 89.7% ± 1.2% without requiring data decryption. By integrating supramolecular materials engineering, wearable sensing device design, and privacy-preserving machine learning strategies, this study establishes a practical framework for secure physiological monitoring and encrypted wearable biometric systems.

DECLARATIONS

Authors' contributions

Conceived the research and supervised all aspects of the work: Jin, Y; Cheng, B; Chen, L.
Provided the physiological characteristics of gait dynamics: Jin, Y; Wang, R; Lu, Y; Lin, J; Zhang, J.
Discussed the device structure and fabrication: Jin, Y; Cheng, B.
Fabricated the multimodal sensor, conducted the measurements, simulated the structures of strain sensor and analyzed the raw data: Jin, Y; Cheng, B; Wang, R.
Conducted the machine learning for gait recognition: Jin, Y.
Prepared the manuscript: Jin, Y; Zhou, X; Cheng, B; Chen, L.
All of the authors read, edited, and approved the final version of the manuscript.

Availability of data and materials

The data supporting the findings of this study are presented in this manuscript and Supplementary Materials.

AI and AI-assisted tools statement

Not applicable.

Financial support and sponsorship

This work was supported by the National Natural Science Foundation of China (Nos. 52275566 and 52505414), and the Jiangsu Provincial Key Laboratory of Advanced Robotics.

Conflicts of interest

All authors declared that there are no conflicts of interest.

Ethical approval and consent to participate

This study adhered to local regulations and ethical standards, involving exclusively non-invasive monitoring of body movements and physiological signals. Since no sensitive personal data were collected and the procedures involved no commercial interests or risk of participant harm, the study was deemed exempt from formal ethical review. All signal tests involving human subjects were conducted with the informed consent of the participants, who are also co-authors of this study.

Consent for publication

Not applicable.

Supplementary Materials

Supplementary Materials

REFERENCES

1. Zeng, L.; Shen, P.; Zhu, X.; Tian, X.; Chen, C. A review of privacy-preserving biometric identification and authentication protocols. *Comput. Secur.* **2025**, *150*, 104309. DOI
2. Alrawili, R.; Alqahtani, A. A. S.; Khan, M. K. Comprehensive survey: Biometric user authentication application, evaluation, and discussion. *Comput. Electr. Eng.* **2024**, *119*, 109485. DOI
3. Nonnekes, J.; Goselink, R. J. M.; Růžička, E.; Fasano, A.; Nutt, J. G.; Bloem, B. R. Neurological disorders of gait, balance and posture: a sign-based approach. *Nat. Rev. Neurol.* **2018**, *14*, 183-9. DOI PubMed
4. Li, J.; Zhang, S.; Zhong, J.; et al. Laser-induced graphene-assisted patterning and transfer of silver nanowires for ultra-conformal breathable epidermal electrodes in long-term electrophysiological monitoring. *Adv. Funct. Mater.* **2025**, *35*, 2504481. DOI
5. Dong, X.; Fan, F.; Chen, L.; et al. Mechanical interlocking enhanced hybrid electrode for long-term epidermal biopotential monitoring in clinical applications. *Chem. Eng. J.* **2026**, *527*, 171609. DOI
6. Xiao, M.; Luo, Y.; Chen, H.; et al. Conformal bioadhesive hydrogel-based multimodal wristband for accurate, mobile, and real-time sign language translation and human-machine interactions. *Adv. Funct. Mater.* **2025**, *36*, e22153. DOI
7. Álvarez-aparicio, C. Guerrero-higueras, Á. M.; González-santamarta, M. Á.; Campazas-vega, A.; Matellán, V.; Fernández-llamas, C. Biometric recognition through gait analysis. *Sci. Rep.* **2022**, *12*, 14530. DOI PubMed PMC
8. Wang, Q.; Guan, H.; Wang, C.; et al. A wireless, self-powered smart insole for gait monitoring and recognition via nonlinear synergistic pressure sensing. *Sci. Adv.* **2025**, *11*, eadu1598. DOI PubMed PMC
9. Sun, R.; Wu, P.; Li, P.; et al. Bio-inspired triboelectric nanogenerator as a self-powered gait recognition sensor for legged robots. *Sci. China. Mater.* **2025**, *68*, 1542-51. DOI
10. Jani, A. B.; Bagree, R.; Roy, A. K. Design of a low-power, low-cost ECG & EMG sensor for wearable biometric and medical application. In *2017 IEEE SENSORS*, Glasgow, UK, October 29-November 1, 2017; IEEE, 2017; pp 1-3. DOI
11. Huang, X.; Zheng, H.; Zhou, Z.; Sheng, Y. Gait recognition based on a-mode ultrasound and inertial sensor fusion systems. In *Intelligent Robotics and Applications, ICIRA 2024,* Xi'an, China, July 31-August 2, 2024; Lan, X., Mei, X., Jiang, C., Zhao, F., Tian, Z., Eds.; Springer: Singapore, 2025; pp 192-205. DOI
12. Chen, Y.; Liu, Z.; Wang, Z.; et al. Bioinspired robust gas-permeable on-skin electronics: armor-designed nanoporous flash graphene assembly enhancing mechanical resilience. *Adv. Sci.* **2024**, *11*, 2402759. DOI PubMed PMC
13. Shi, X.; Song, D.; Hu, W.; et al. A sweat absorbing skin electrode for electrophysiology during exercise. *Adv. Funct. Mater.* **2024**, *34*, 2314775. DOI
14. Liu, Y.; Chen, S.; Shi, L.; et al. Water-enhanced adhesive interface for high-quality physiological signal monitoring in skin-device integration. *Adv. Funct. Mater.* **2025**, *36*, e16396. DOI
15. He, Y.; Cheng, Y.; Yang, C.; Guo, C. F. Creep-free polyelectrolyte elastomer for drift-free iontronic sensing. *Nat. Mater.* **2024**, *23*, 1107-14. DOI PubMed
16. He, J.; Huang, J.; Li, R.; et al. Hysteresis-free and dynamically resilient strain sensor enabled by interfacial coordination. *Sci. Adv.* **2026**, *12*, eaea2450. DOI PubMed PMC
17. Yang, J. C.; Mun, J.; Kwon, S. Y.; Park, S.; Bao, Z.; Park, S. Electronic skin: recent progress and future prospects for skin-attachable devices for health monitoring, robotics, and prosthetics. *Adv. Mater.* **2019**, *31*, 1904765. DOI PubMed
18. Ohm, Y.; Pan, C.; Ford, M. J.; Huang, X.; Liao, J.; Majidi, C. An electrically conductive silver-polyacrylamide-alginate hydrogel composite for soft electronics. *Nat. Electron.* **2021**, *4*, 185-92. DOI
19. Sun, T.; Feng, B.; Huo, J.; et al. Artificial intelligence meets flexible sensors: emerging smart flexible sensing systems driven by machine learning and artificial synapses. *Nano-Micro. Lett.* **2023**, *16*, 14. DOI PubMed PMC
20. Song, Y.; Liu, Y.; Qi, T.; Li, G. L. Towards dynamic but supertough healable polymers through biomimetic hierarchical hydrogen-bonding interactions. *Angew. Chem. Int. Ed.* **2018**, *57*, 13838-42. DOI PubMed
21. Jeon, I.; Cui, J.; Illeperuma, W. R. K.; Aizenberg, J.; Vlassak, J. J. Extremely stretchable and fast self-healing hydrogels. *Adv. Mater.* **2016**, *28*, 4678-83. DOI PubMed

22. Liu, K.; Cheng, L.; Zhang, N.; et al. Biomimetic impact protective supramolecular polymeric materials enabled by quadruple H-bonding. *J. Am. Chem. Soc.* **2020**, *143*, 1162-70. DOI PubMed
23. Jin, Y.; Wang, R.; Tang, D.; et al. AI-enabled adaptive eutectogel skin for effective motion monitoring with low signal artifacts. *Adv. Funct. Mater.* **2025**, *35*, 2424965. DOI
24. Jiang, W. J.; Zhong, F. Y.; Zhou, L. S.; Peng, H. L.; Fan, J. P.; Huang, K. Chemical dual-site capture of NH_3 by unprecedentedly low-viscosity deep eutectic solvents. *Chem. Commun.* **2020**, *56*, 2399-402. DOI PubMed
25. Guo, X.; Zhang, S.; Patel, S.; et al. A skin-mimicking multifunctional hydrogel via hierarchical, reversible noncovalent interactions. *Sci. Adv.* **2025**, *11*, eadv8523. DOI PubMed PMC
26. Xiang, H.; Li, X.; Wu, B.; Sun, S.; Wu, P. Highly damping and self-healable ionic elastomer from dynamic phase separation of sticky fluorinated polymers. *Adv. Mater.* **2023**, *35*, 2209581. DOI PubMed
27. Yu, T.; Zhang, L.; Dou, X.; et al. Mechanically robust hydrogels facilitating bone regeneration through epigenetic modulation. *Adv. Sci.* **2022**, *9*, 2203734. DOI PubMed PMC
28. Zhu, R.; Zhu, D.; Zheng, Z.; Wang, X. Tough double network hydrogels with rapid self-reinforcement and low hysteresis based on highly entangled networks. *Nat. Commun.* **2024**, *15*, 1344. DOI PubMed PMC
29. Li, W.; Wang, X.; Liu, Z.; et al. Nanoconfined polymerization limits crack propagation in hysteresis-free gels. *Nat. Mater.* **2023**, *23*, 131-8. DOI PubMed
30. Yang, K.; Li, Q.; Tian, S.; et al. Highly stretchable, self-healing, and sensitive e-skins at -78 °C for polar exploration. *J. Am. Chem. Soc.* **2024**, *146*, 10699-707. DOI PubMed
31. Sun, H.; Lee, H. H.; Blakey, I.; et al. Multiple hydrogen-bonded complexes based on 2-ureido-4[1*H*]-pyrimidinone: a theoretical study. *J. Phys. Chem. B.* **2011**, *115*, 11053-62. DOI PubMed
32. Fengler, C.; Keller, J.; Ratzsch, K. F.; Wilhelm, M. *In situ* RheoNMR correlation of polymer segmental mobility with mechanical properties during hydrogel synthesis. *Adv. Sci.* **2021**, *9*, 2104231. DOI PubMed PMC
33. Dong, J.; Liu, H.; Lim, T.; et al. Viscoelastic adhesive, super-conformable, and semi-flowable liquid metal eutectogels for high-fidelity electrophysiological monitoring. *ACS. Appl. Mater. Interfaces.* **2024**, *16*, 34732-42. DOI PubMed
34. Liu, P.; Pei, D.; Wu, Y.; Li, M.; Zhao, X.; Li, C. Dynamic and mechanically robust and ultrafast healable ionogel for nerve fiber-inspired signal transmitter. *J. Mater. Chem. A.* **2022**, *10*, 25602-10. DOI
35. Noda, I. Generalized two-dimensional correlation method applicable to infrared, Raman, and other types of spectroscopy. *Appl. Spectrosc.* **1993**, *47*, 1329-36. DOI
36. Yang, J.; Chang, L.; Deng, H.; Cao, Z. Zwitterionic eutectogels with high ionic conductivity for environmentally tolerant and self-healing triboelectric nanogenerators. *ACS. Nano.* **2024**, *18*, 18980-91. DOI PubMed
37. Lata, K.; Saini, S. Hardware software co-simulation of an AES-128 based data encryption in image processing systems for the internet of things environment. In *2020 IEEE International Symposium on Smart Electronic Systems (iSES) (Formerly iNiS)*, Chennai, India, December 14-16, 2020; IEEE, 2020; pp 260-4. DOI